Applied Catalysis B: Environmental 168-169 (2015) 266–273

Contents lists available at ScienceDirect

Applied Catalysis B: Environmental

journal homepage: www.elsevier.com/locate/apcatb

# Cross-linked $ZnIn_2S_4$/rGO composite photocatalyst for sunlight-driven photocatalytic degradation of 4-nitrophenol

Jiangyao Chen[a,b], Haimin Zhang[a], Porun Liu[a], Yibing Li[a], Xiaolu Liu[a], Guiying Li[b], Po Keung Wong[c], Taicheng An[b,*], Huijun Zhao[a,**]

[a] Centre for Clean Environment and Energy, Griffith University, Gold Coast Campus, Qld 4222, Australia
[b] The State Key Laboratory of Organic Geochemistry and Guangdong Key Laboratory of Environmental Protection and Resources Utilization, Guangzhou Institute of Geochemistry, Chinese Academy of Sciences, Guangzhou 510640, China
[c] School of Life Sciences, The Chinese University of Hong Kong, Shatin, NT, Hong Kong SAR, China

ARTICLE INFO

*Article history:*
Received 2 December 2014
Received in revised form
27 December 2014
Accepted 30 December 2014
Available online 2 January 2015

*Keywords:*
Graphene
Ternary sulfides
Cross-link
Sunlight-driven photocatalysis
4-Nitrophenol

ABSTRACT

A chemically cross-linked $ZnIn_2S_4$/reduced graphene oxide (ZIS/rGO) composite photocatalyst was synthesized as a stable sunlight photocatalyst for the degradation of 4-nitrophenol. The experimental results revealed that although the pure $ZnIn_2S_4$ exhibited reasonable visible light photocatalytic activity toward the degradation of 4-nitrophenol, it was suffered from severe photocorrosion under sunlight irradiation. In strong contrast, the chemically cross-linked ZIS/rGO possessed not only an enhanced visible light photocatalytic activity but also a dramatically improved sunlight stability. The characterization data suggested that $ZnIn_2S_4$ nanosheet was chemically interacted with rGO sheet through Zn—O—C covalent bonds, leading to a tunable band structure and enhanced photocatalytic activity. More importantly, such covalent bondings between $ZnIn_2S_4$ and rGO could improve the composite's structural stability, capable of dramatically enhancing the photocorrosion resistance under sunlight irradiation. The findings of this work would provide a new means for design of visible light active and sunlight stable photocatalysts for environmental remediation applications.



## 1. Introduction

As a green technology, heterogeneous photocatalysis has demonstrated a great potential for environmental remediation applications [1,2]. However, the most reported semiconductor photocatalysts to date are active only under UV light illumination, greatly limited their practical applications. Extensive efforts have therefore been devoted to develop visible light active photocatalysts, resulting in a large number of visible light active photocatalysts being synthesized [3–5]. However, a key issue remains unresolved, that is, most of reported visible light active photocatalysts are unstable under sunlight irradiation due to the severe photocorrosion caused by the UV component of the sunlight [6–9]. In order to practically utilize sunlight-driven photocatalysis, a photocatalyst must be not only visible light active but also stable under sunlight irradiation.

$ZnIn_2S_4$, a ternary semiconductor chalcogenide with a narrow bandgap (2.34–2.48 eV), well corresponding to the visible light region, has attracted great interest for visible light-driven photocatalytic degradation of organic pollutants and water splitting to produce hydrogen [10–14]. However, as a photocatalyst, the $ZnIn_2S_4$ suffers a critical drawback of high photocorrosion under sunlight irradiation, which in fact is a general issue for most of narrow bandgap semiconductors [15]. For example, the metal sulfide semiconductors with narrow bandgaps such as CdS possess high activity, reasonable stability and photocorrosion resistance under visible light irradiation. However, they become unstable when subjected to sunlight irradiation [16].

Recently, graphene has received considerable attention due to its unique optical, electronic and mechanical properties, promising for a wide range of applications [17,18]. More recently, a number of reports have indicated that the photocatalytic performance of semiconductor materials can be significantly improved when composited with graphene [19–23]. Importantly, some wide bandgap semiconductors (*e.g.*, $TiO_2$) could exhibit visible light activity after composited with graphene [18,19,24,25]. This is attributed to the advantageous properties of graphene such as visible light absorptivity, superior electron transport ability within the

* Corresponding author. Tel.: +86 20 85291501; fax: +86 20 85290706.
** Corresponding author. Tel.: +61 7 55528261; fax: +61 7 55528067.
*E-mail addresses:* antc99@gig.ac.cn (T. An), h.zhao@griffith.edu.au (H. Zhao).

http://dx.doi.org/10.1016/j.apcatb.2014.12.048
0926-3373/

photocatalysts, and suppressed charge recombination and tuned band structure can be induced into the semiconductor/graphene composites [18,19,26,27]. More importantly, the narrow bandgap semconductor/graphene composite photocatalysts have shown an increased photocorrosion resistance with enhanced photostability [6]. For example, several groups have demonstrated that the reduced graphene oxide (rGO)–$ZnIn_2S_4$ composites possess the enhanced visible light photocatalytic activity and stability for the solar hydrogen production [28,29], and pollutants degradation [30]. However, to the best of our knowledge, fabricating narrow bandgap semiconductor/rGO composite photocatalysts with chemically cross-linked semiconductor and graphitic carbon bonding to improve the sunlight stability has not been previously reported.

Herein, $ZnIn_2S_4$/rGO (ZIS/rGO) composites with Zn—O—C cross-linked bonds were synthesized to improve the visible light photocatalytic activity and the sunlight stability. The enhanced photocatalytic performance was due largely to the existence of the cross-linked covalent bonds between inorganic component and rGO, which was differing remarkably from the reported approaches for which the composite was formed via non-covalent bonding. The readily tunable optical property and band structure of the resulting composite *via* simple control of the amount of GO enabled the control synthesis of the composite with high photocatalytic activity and excellent solar stability. The photocatalytic performance of the resultant ZIS/rGO composite photocatalysts was systematically investigated using 4-nitrophenol (4-NP) as a model contaminant under both visible light and simulated sunlight irradiations. The selection of 4-NP as the model contaminant was because of its environmental importance. As well known, 4-NP was a highly toxic compound which was widely used as intermediates for synthesis of pesticides, insecticides, herbicides and dyes [31]. The widespread use and high solubility made 4-NP often present in industrial and environmental waters, potentially causing severe chronic poisoning even at very low concentrations.

## 2. Experimental

### 2.1. Synthesis

Graphene oxide (GO) was synthesized by modified Hummers method through the oxidation of graphite powder, as reported in our previous report [18]. For synthesis of ZIS/rGO composite, a certain amount of GO was dispersed into a 10 mL of distilled water by ultrasonication for 30 min. Then, 0.147 g $InCl_3{\cdot}4H_2O$, 0.072 g $ZnSO_4{\cdot}7H_2O$ and 0.150 g $C_2H_5NS$ was added into the above solution under stirring. The formed mixture was then stirred for another 30 min. Finally, the obtained solution was transferred into a 15 mL Teflon-lined stainless steel autoclave, and heated to 180 °C for 12 h. After the hydrothermal reaction, the as-synthesized products were obtained by centrifuged, rinsed adequately with distilled water and then dried at 60 °C for 12 h in a vacuum oven. The obtained composite was denoted as ZIS/rGO-X%, where X% is the initial weight ratio of GO. For comparison, $ZnIn_2S_4$ and rGO were also fabricated with the same method.

### 2.2. Characterization

X-ray diffraction (XRD, Shimadzu XRD-6000 diffractometer, equipped with a graphite monochromator) was employed to characterize the crystal structure. Raman spectra were recorded on a Renishaw inVia Raman microscope with a laser excitation wavelength of 520 nm. Morphology and microstructures of the samples were observed by the scanning electron microscopy (SEM, JEOL JSM-6300F) and transmission electron microscopy (TEM, Philips F20), and the elemental mapping was characterized by JEOL 7001 scanning electron microscopy. The specific surface areas of the materials were calculated using the Brunauer–Emmett–Teller method. UV–visible (UV–vis) diffuse reflectance spectra of the samples were recorded on a UV–vis-NIR spectrophotometer (Varian Cary 300). Chemical compositions of the prepared composites were analysed by X-ray photoelectron spectroscopy (XPS, Kratos Axis ULTRA incorporating a 165 mm hemispherical electron energy analyser). Fourier transform infrared spectroscopy (FT-IR, PerkinElmer spectrum 1000) analysis of the composite was performed using FT-IR spectrophotometer (KBr as the reference sample). Photoluminescence spectra (PL, Hitachi F-7000, excitation wavelength: 330 nm, scanning rate: 1200 nm $min^{-1}$, PMT voltage: 500 V, widths of the excitation slit and emission slit: 20 nm) of the composites were obtained using a fluorescence spectrometer at 293 K.

### 2.3. Photocatalytic activity and stability measurement

The visible light (VL) photocatalytic activity was evaluated in a XPAII photoreactor (Nanjing Xujiang Machineelectronic Plant, China). 100 mg of photocatalyst was put into 60 mL of quartz test tube containing 50 mL of 10 mg $L^{-1}$ 4-NP, and then stirred in dark for 30 min to achieve adsorption equilibrium before light irradiation. After that, a 1000 W Xe lamp was used as the VL source (the UV light was cut off by 2.0 M sodium nitrite [18]) to perform the photocatalytic experiment at 25 °C. Under simulated sunlight (SSL) irradiation, a 500 W Xe lamp (Trusttech Co., Beijing) with an AM 1.5 G filter (Sciencetech, Canada) was used as the light source. The incident visible-light and solar-light intensity were 82 and 100 mW $cm^{-2}$, respectively. The remaining concentration of 4-NP in reaction solution was determined using the UV–vis spectrophotometer (UV-1800, Shimadu). To determine the extent of mineralization, total organic carbon (TOC) contents of solution were measured with a Shimadzu $TOC-_{VCPH/CPN}$ analyzer. To evaluate the photostability, the photocatalyst after the first run of 360 min for VL irradiation (or 180 min for SSL irradiation) was separated by centrifuged from the suspension, washed with water, and dried at 60 °C, and then, the recovered photocatalyst was reused for the next run of the photocatalytic degradation under the same conditions.

## 3. Results and discussion

### 3.1. Structural characteristics

XRD patterns of the prepared composites are shown in Figs. 1A and S1. As can be seen, $ZnIn_2S_4$ and ZIS/rGO composites show the same diffraction peaks of (0 0 6), (1 0 2), (1 0 4), (1 0 8), (1 1 0), (1 1 6) and (2 0 0) crystal planes at $2\theta = 21.6°$, 27.7°, 30.4°, 39.8°, 47.2°, 52.4° and 55.0°, respectively, which can be indexed to a hexagonal phase of $ZnIn_2S_4$ (JCPDS NO. 65-2023), indicating that low content of GO added (≤wt. 3.0% in our case) has no significant influence on the crystal phase of $ZnIn_2S_4$ in composite. The presence of rGO in composite can be confirmed by Raman spectra, and two typical peaks are found to be located at 1340 and 1590 $cm^{-1}$, corresponding to D and G bands, respectively (Fig. 1B). For ZIS/rGO–1.5%, besides these two peaks, two new characteristic peaks at around 250 and 355 $cm^{-1}$ attributed to the typical stretching modes of $ZnIn_2S_4$ can also be observed [28], confirming the existence of both $ZnIn_2S_4$ and GO in the composite. Furthermore, an increased D/G intensity ratio ($I_D/I_G = 1.16$) for ZIS/rGO–1.5% is also obtained in comparison with that of GO ($I_D/I_G = 0.88$), indicating that the GO has been, to some extent, reduced to rGO during the hydrothermal process.

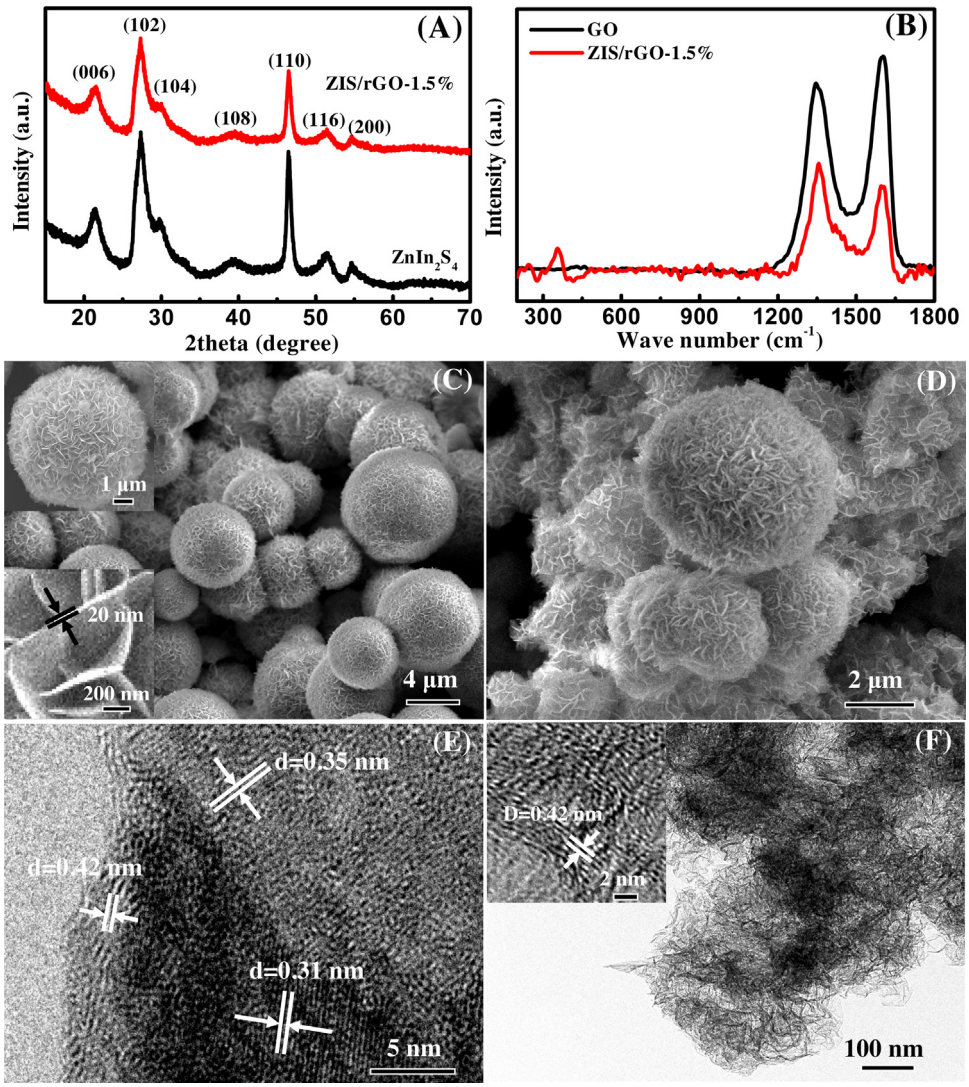


**Fig. 1.** XRD patterns (A) and Raman spectra (B) of $ZnIn_2S_4$ and ZIS/rGO-1.5%. SEM images of $ZnIn_2S_4$ (C) and ZIS/rGO-1.5% (D) TEM images of ZIS/rGO-1.5% (E) and rGO (F).

To further investigate the effect of GO weight ratio on the morphology and microstructure of the composites, as-synthesized rGO, $ZnIn_2S_4$ and ZIS/rGO composites are characterized by SEM and TEM techniques. SEM results reveal that $ZnIn_2S_4$ exhibits microsphere structure of 4–8 μm in diameter (Fig. 1C), which is composed of numerous nanosheets with the thickness of *ca.* 20 nm (inset in Fig. 1C). The ZIS/rGO composite shows a mixture of microspheres and dispersed nanosheets, while the amount and size of microsphere apparently decrease and the dispersed nanosheets become dominant species with the increase of the amount of GO added (Figs. 1D and S2), implying that resulted rGO can act as a structure-directing agent transforming $ZnIn_2S_4$ structure from microsphere into nanosheet. Similar results can also be found in other graphene based composites [32,33]. The $ZnIn_2S_4$ microspheres before and after rGO modification both show solid structure (TEM data not shown) and the HRTEM image of ZIS/rGO–1.5% exhibits two sets of lattice fringes (Fig. 1E). One is ordered with different interlayer distances (d-spacing) of 0.31 and 0.35 nm, and the other is not well defined with d-spacing of around 0.42 nm. The former one corresponds to the (1 0 3) and (0 0 7) planes of hexagonal $ZnIn_2S_4$, while the later one can be assigned to the (0 0 2) plane of rGO as the pure rGO obtained under the same experimental conditions shows the same d-spacing (Fig. 1F). It should be noted that the measured value (around 0.42 nm) of the d-spacing of rGO in this composite is a slightly larger than that of perfectly crystallized graphite (0.34 nm), which may be attributed to the presence of oxygen-containing groups [32,34]. Moreover, the elemental mapping analysis of ZIS/rGO–1.5% displayed in Fig. S3 suggests the homogeneous distribution of C, O, Zn, In and S elements in the composite, indicating the coexistence of $ZnIn_2S_4$ and rGO in the composite. Therefore, based on the above analysis, it is concluded that rGO sheet effectively binds with $ZnIn_2S_4$ nanosheet, which may be beneficial for improving the photocatalytic performance and stability of the resulting composite. Furthermore, $N_2$ adsorption–desorption isotherms and the corresponding pore size distribution curves of $ZnIn_2S_4$ and ZIS/rGO composites are also investigated and similar type IV (IUPAC classification) isotherms are observed for all samples with a typical H3 hysteresis loop [35], indicating the existence of mesoporous structure and slit-like pores (Fig. 2A). The corresponding pore size distributions of the samples are wide in the range of 2–40 nm, further confirming the presence of a large number of mesopores (Fig. 2B). The calculated specific surface areas are 72.9, 73.5, 72.8, 71.4 and 51.8 $m^2\ g^{-1}$ for $ZnIn_2S_4$, ZIS/rGO–0.30%, ZIS/rGO–0.75%, ZIS/rGO–1.5% and ZIS/rGO–3.0%, respectively. Apparently, high surface area of the composite can be remained close to that of $ZnIn_2S_4$ when the initial weight ratio of GO is below 1.5%, while the surface area significantly decreases with further increasing the amount of GO. The above results reveal that

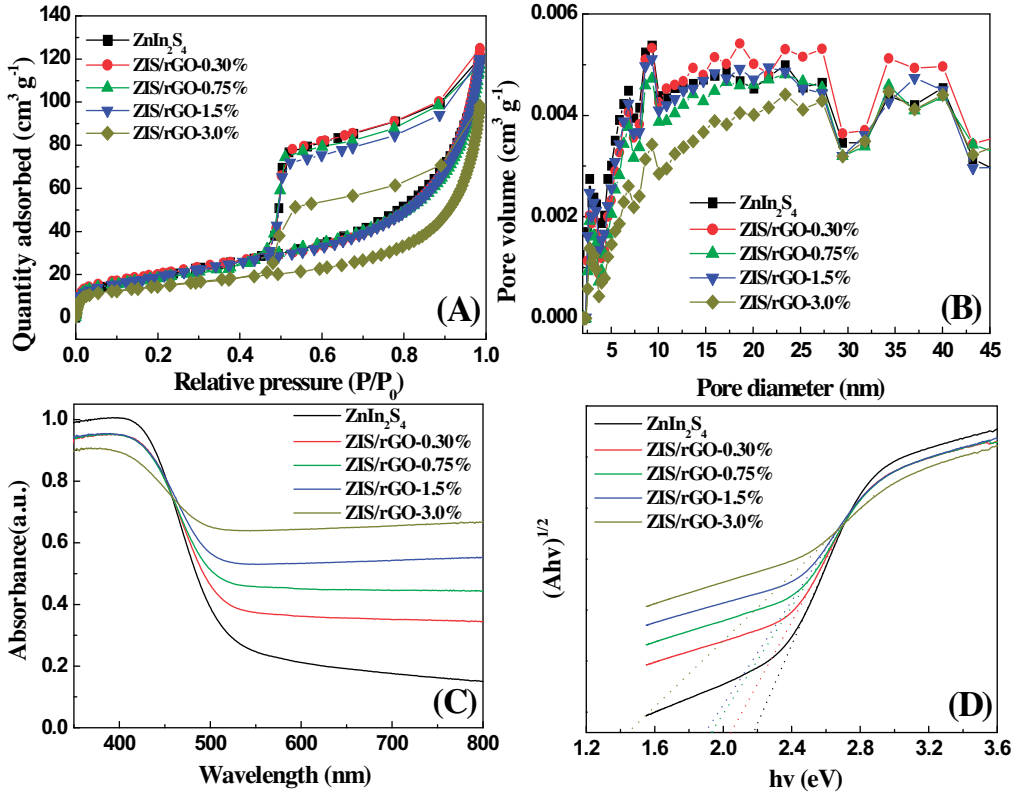


**Fig. 2.** $N_2$ adsorption-desorption isotherms (A) and pore size distribution curves (B) of $ZnIn_2S_4$ and ZIS/rGO composites. UV–vis diffuse reflectance spectra (C) and the plots of transformed Kubelka–Munk function versus the light energy (D) of $ZnIn_2S_4$ and ZIS/rGO composites.

the nanosheet assembled microsphere structure should contribute to the high surface area of $ZnIn_2S_4$ and ZIS/rGO composites.

Based on the above results, it can be concluded that with a suitable initial weight ratio of GO added, the resulted rGO modification not only adjusts the morphology of the resulting composite, but also changes the microstructure of the composite, thus resulting in significant difference in the surface area. Similar results have also been reported by Kumar et al. and Ma et al. [33,36].

### 3.2. Optical characteristics

Besides the structural properties, the rGO modification also significantly affects the optical property of $ZnIn_2S_4$. As shown in Fig. 2C, all investigated samples exhibit strong VL light absorption. In comparison with $ZnIn_2S_4$, the ZIS/rGO composites exhibit significantly improved VL absorption capability with increasing the initial weight ratio of GO. Importantly, with increasing the amount of GO added, a red shift of the absorption band edge to a longer wavelength is observed, indicating the bandgap narrowing of ZIS/rGO composite. Similar observation has also been reported for other rGO modified composites [18,37]. Based on UV–vis diffuse reflectance spectra, the estimated bandgaps are calculated to be *ca.* 2.17, 2.06, 1.95, 1.92 and 1.45 eV for $ZnIn_2S_4$, ZIS/rGO–0.30%, ZIS/rGO–0.75%, ZIS/rGO–1.5% and ZIS/rGO–3.0%, respectively (Fig. 2D). Some studies have revealed that for rGO modified semiconductor photocatalysts (*e.g.*, $TiO_2$/rGO and $C_3N_4$/rGO), the formation of the chemical bonding between semiconductor material (*e.g.*, $TiO_2$ or $C_3N_4$) and the specific sites of rGO (*e.g.*, Ti—O—C or C—O—C bonding), leading to a red shift of the absorption band edge of the composite [18,19]. In this study, similar to these rGO modified composites, the oxygen-rich active sites on GO surface (*e.g.*, —OH, —COOH) may play key role of cross-linkers to form Zn—O—C covalent bonding rGO sheet with $ZnIn_2S_4$ nanosheet during the hydrothermal reaction, which may be the reason why the band structure can be easily tuned in this study. This hypothesis can be further confirmed by the results of XPS and FT-IR analysis.

The XPS surface survey spectrum shows the presence of C1s, Zn2p, In3d, S2p and O1s peaks in the composite (Fig. S4). The presence of O1s peak is due to the residual oxygen-containing groups in rGO, which is well agreed with Pan et al. report [32]. The high-resolution XPS spectra analysis of Zn, In and S elements indicates that the atomic ratio of Zn2p, In3d, and S2p is close to be 1:2:4, meaning the formation of $ZnIn_2S_4$ (Fig. S5). Fig. 3A shows the high resolution C1s spectrum of GO, where three peaks of C1s can be deconvoluted. The peak at 284.6 eV is attributed to sp2 carbon atom (C—C, C=C and C—H groups), while the peak cantered at 286.7 eV is assigned to the C from the C—OH and C=O groups [38]. The peak located at 288.5 eV is closely associated with the O=C—OH species [39]. Compared with the C1s spectrum of GO, the peaks of C—OH, C=O and O=C—OH for ZIS/rGO–1.5% still exist with decreased peak intensity, implying the substantial reduction of GO after the hydrothermal reaction (Fig. 3B). Meanwhile, a new peak at 287.6 eV can be observed, which is attributed to the Zn—O—C bond [40]. Furthermore, the FT-IR spectrum of GO shows C=O (1724 cm$^{-1}$), aromatic C=C (1621 cm$^{-1}$) and alkoxy C—OH stretches (1049 cm$^{-1}$) (Fig. 3C) [28,41]. Similarly, the FT-IR spectrum of ZIS/rGO–1.5% composite also shows two obvious peaks at 1742 (C=O) and 1628 (C=C) with decreased peak intensity, again indicating the incompletely hydrothermal reduction of GO. Further observation indicates that the peak of C—OH at 1049 cm$^{-1}$ almost disappears, while a new peak at 1091 cm$^{-1}$ assigned to Zn—O—C can be discerned (Fig. 3D) [42], which means that C—OH groups may act as cross-linkers to form Zn—O—C bonds in the composite during the hydrothermal reaction (Fig. S6). And the formed ZnOC bonds should be responsible for the bandgap narrowing of the composite [18,40]. Moreover, the residual oxygen-containing groups may induce an

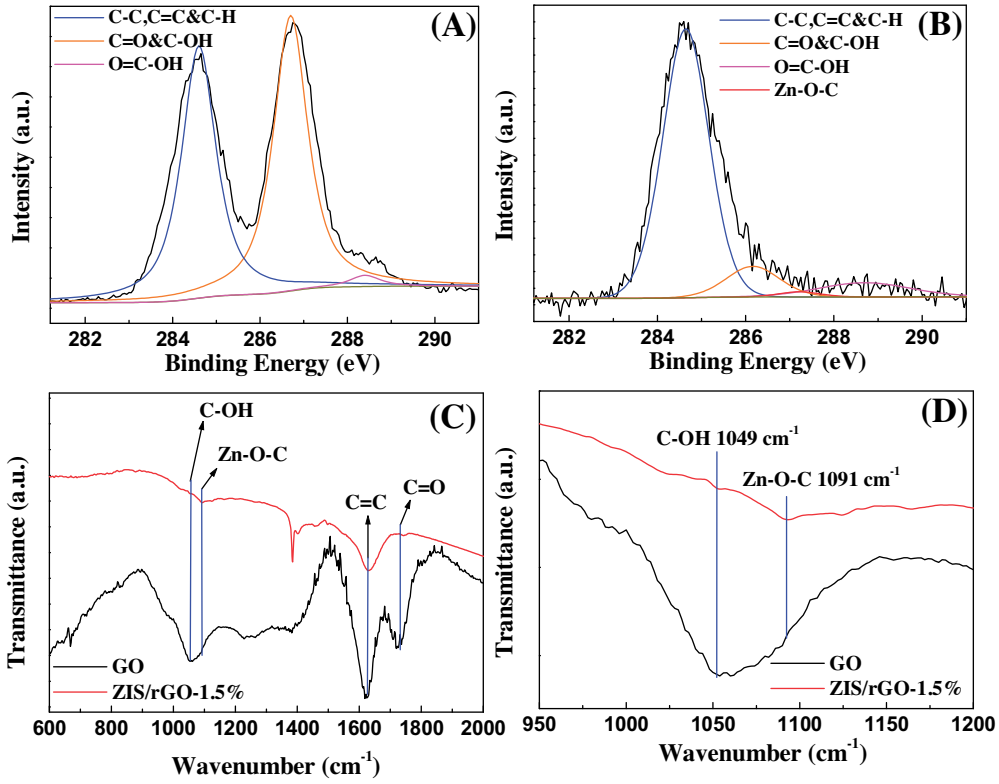


**Fig. 3.** High resolution C1s XPS spectra of GO (A) and ZIS/rGO–1.5% (B), and FT-IR spectra of GO (C) and ZIS/rGO–1.5% (D).

increase in interplanar distance of the resulted rGO, leading to the d-spacing of rGO slightly larger than that of perfectly crystallized graphite, which is also consistent with the TEM results.

To further investigate the effect of the addition amount of GO on the band structure of the ZIS/rGO composite, the flat band potentials of $ZnIn_2S_4$ and ZIS/rGO composites are measured by electrochemical technique to approximately estimate their conduction band edge potentials ($E_{cb}$), with a method as addressed in literatures [18,43]. The $E_{cb}$ potentials derived from Mott–Schottky plots are about −0.79, −0.66, −0.54, −0.40 and −0.38 V for $ZnIn_2S_4$, ZIS/rGO–0.30%, ZIS/rGO–0.75%, ZIS/rGO–1.5%, and ZIS/rGO–3.0%, respectively (Fig. 4A). Obviously, the conduction band edge potentials of ZIS/rGO composites become positive-shift compared to $ZnIn_2S_4$. Based on the bandgap values of the samples obtained by UV–vis diffuse reflectance spectra (Fig. 2D), the valence band edge potentials ($E_{vb}$) are calculated as *ca.* 1.38, 1.40, 1.41, 1.52 and 1.07 V for $ZnIn_2S_4$, ZIS/rGO–0.30%, ZIS/rGO–0.75%, ZIS/rGO–1.5% and ZIS/rGO–3.0%, respectively (Fig. 4B). Compared to $ZnIn_2S_4$, the $E_{vb}$ of the ZIS/rGO–0.30%, ZIS/rGO–0.75% and ZIS/rGO–1.5% apparently become positive-shift, while a negative-shift of $E_{vb}$ occurs for ZIS/rGO–3.0%. And ZIS/rGO–1.5% displays the most positive valence band potential, meaning the highest oxidation power in comparison with other samples.

### 3.3. Photocatalytic activity and stability evaluation

To evaluate the photocatalytic activity of the prepared samples, the photocatalytic degradation of 4-NP is firstly carried out under VL irradiation (λ > 400 nm). Fig. 5A shows the VL photocatalytic degradation curves of 4-NP by $ZnIn_2S_4$ and ZIS/rGO composites. For control experiments, no adsorption of 4-NP is found without light and photocatalyst, while under VL irradiation, no noticeable degradation of 4-NP is observed with direct photolysis. When both photocatalyst and VL are present, a significant decrease of 4-NP concentration is observed. After 360 min irradiation, approximate 77.1%, 80.0%, 81.8%, 97.8%

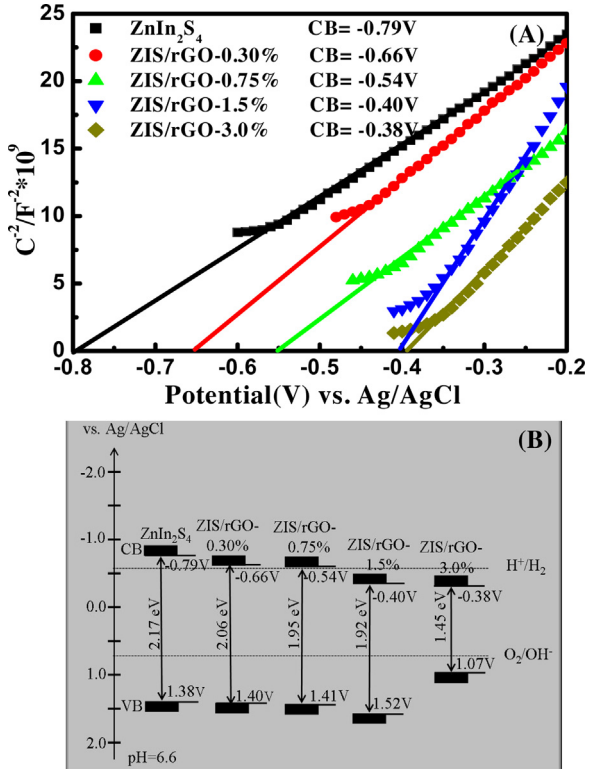


**Fig. 4.** (A) Mott–Schottky plots of $ZnIn_2S_4$ and ZIS/rGO composites at a fixed frequency of 80 Hz. (B) Schematic diagram of band structures (CB: conduction band, VB: valence band) of $ZnIn_2S_4$ and ZIS/rGO composites.

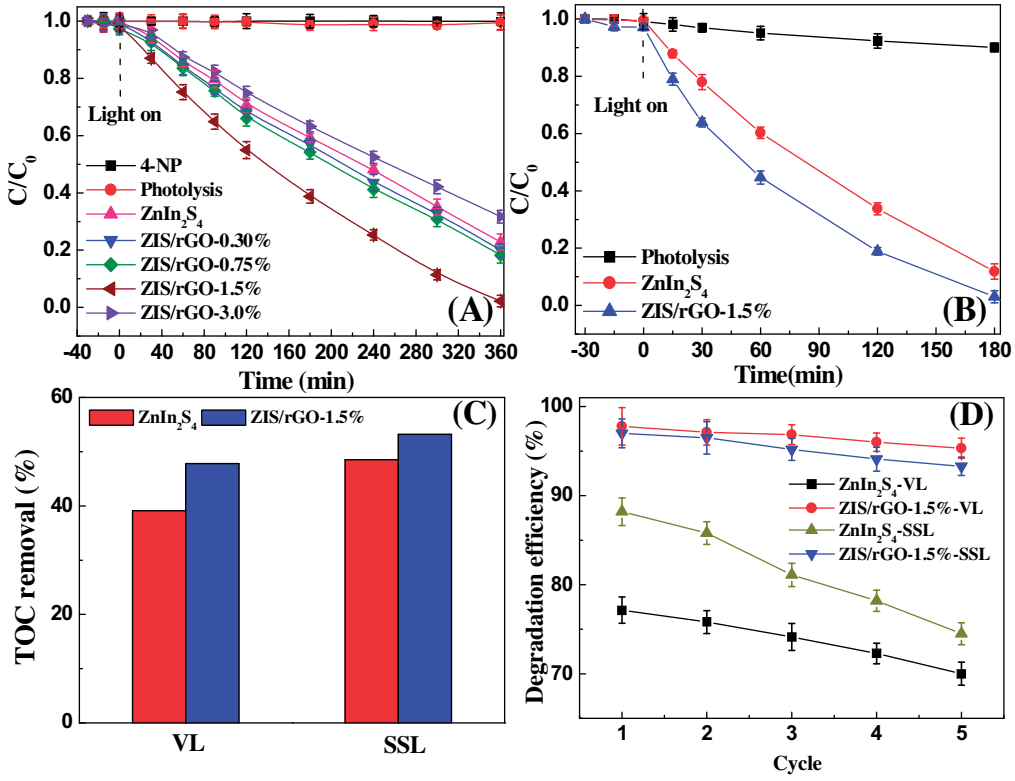


**Fig. 5.** Photocatalytic activity of $ZnIn_2S_4$ and ZIS/rGO composites for the degradation of 4-NP under VL (A) and SSL (B) irradiation, (C) TOC removal efficiency of 4-NP by $ZnIn_2S_4$ and ZIS/rGO–1.5%, (D) Photocatalytic stability test of $ZnIn_2S_4$ and ZIS/rGO–1.5% toward 4-NP degradation.

and 68.3% of 4-NP are degraded by $ZnIn_2S_4$, ZIS/rGO–0.30%, ZIS/rGO–0.75%, ZIS/rGO–1.5%, and ZIS/rGO–3.0%, respectively, and the highest degradation activity can be obtained with ZIS/rGO–1.5% photocatalyst. Moreover, it is found that the photocatalytic degradation of 4-NP follows a pseudo-first-order reaction and the degradation rate by ZIS/rGO–1.5% is almost 2.0 times to $ZnIn_2S_4$, and 1.6, 1.5 and 2.1 times to ZIS/rGO–0.30%, ZIS/rGO–0.75% and ZIS/rGO–3.0% under the same experimental conditions, respectively, which further confirms ZIS/rGO–1.5% exhibiting the highest photocatalytic degradation rate (Fig. S7) and demonstrates that a suitable rGO modification can efficiently promote the photocatalytic activity of $ZnIn_2S_4$.

Furthermore, the photocatalytic activities of $ZnIn_2S_4$ and ZIS/rGO–1.5% composite are investigated under SSL irradiation. As shown in Fig. 5B, only *ca.* 10% of 4-NP is photodegraded within 180 min. When the photocatalyst is added, the degradation efficiency greatly increases to 88.2% and 97.0% for $ZnIn_2S_4$ and ZIS/rGO–1.5%, respectively. Obviously, ZIS/rGO–1.5% composite displays higher photocatalytic activity to 4-NP under both VL and SSL irradiation in comparison with $ZnIn_2S_4$. To further elucidate the environment fate of 4-NP, the extent of mineralization is quantified by the decrease of TOC concentration (Fig. 5C). As seen from the figure, for $ZnIn_2S_4$ photocatalyst, under irradiated by VL for 10 h and SSL for 6 h, about 39.1% and 48.5% of carbon contents in 4-NP solution is mineralized and completely converted into $CO_2$, which are lower than those of ZIS/rGO–1.5% (47.8% and 53.2%), further indicating the enhanced photocatalytic performance of $ZnIn_2S_4$ with rGO modification. It should also be noted that ZIS/rGO–1.5% shows higher photocatalytic and mineralization performances toward 4-NP under SSL irradiation than that under VL irradiation, which may be attributed to the broad-spectra of sunlight, especially the involvement of UV light and indicates that the ZIS/rGO composite is a potential sunlight-driven photocatalyst.

Meanwhile, the stability of a given photocatalyst is a crucial factor for its practical application. More importantly, narrow bandgap semiconductors have been reported more unstable when subjected to sunlight irradiation in comparison with that under visible light irradiation [16]. Thus, the stability test is evaluated and compared by repeatedly photocatalytic degradation of 4-NP using $ZnIn_2S_4$ and ZIS/rGO-1.5% as photocatalysts under both VL and SSL irradiation (Fig. 5D). The result demonstrates that for $ZnIn_2S_4$ under VL irradiation, the degradation efficiency decreases about 7.2% after five repeated use, which increases to *ca.* 13.7% when subjected to SSL irradiation, confirming more unstable of $ZnIn_2S_4$ under SSL irradiation. In comparison, relatively slow and similar decrease of the degradation efficiency for ZIS/rGO–1.5% is observed, and only *ca.* 2.5% and *ca.* 3.7% decrease of the degradation efficiency is obtained under VL and SSL irradiation, suggesting the improved sunlight stability of $ZnIn_2S_4$ after rGO modification. These results indicate that the synthesized ZIS/rGO composite is stable under sunlight, which are more promising in practical photocatalysis application in environmental remediation.

### 3.4. Enhancement mechanism of photocatalytic activity and stability

Based on the above results, it is obvious that a suitable amount of GO added can significantly improve the photocatalytic performance including the activity and the stability of ZIS/rGO composite compared with $ZnIn_2S_4$. This improved photocatalytic performance of the composite with an optimized amount of GO added can be attributed to the synergistic effect of following advantages: narrowed bandgap, positive valence band potential and superior electron transport property ascribed from the formation of Zn—O—C bonds as well as relatively high surface area. Fig. 6 displays the schematic diagram of the enhanced photocatalytic mechanism over

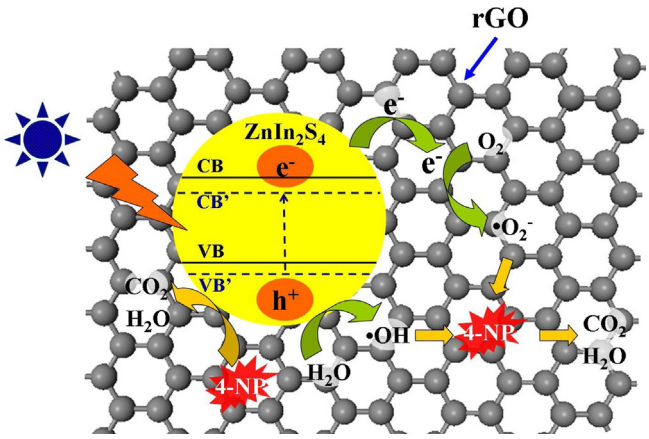


**Fig. 6.** Schematic diagram of the enhanced photocatalytic mechanism over ZIS/rGO composite.

ZIS/rGO composite. When it subjected to light irradiation, due to the formation of the Zn—O—C bonds between $ZnIn_2S_4$ nanosheet and rGO sheet, the bandgap of ZIS/rGO composite is further narrowed, leading to the improvement of the utilization of VL. Meanwhile, more positive valence band potential is obtained after rGO modification, providing the higher photocatalytic oxidation ability of composite toward 4-NP. Besides, the photogenerated electrons can transfer quickly from $ZnIn_2S_4$ conduction band to rGO through the Zn—O—C bonds, which could subsequently suppress the charge recombination and lead to the increase in the number of holes participating in the photocatalytic reaction. Moreover, the excellent electron mobility of graphene sheet increases the charge transport rate and achieves enhanced charge separation subsequently accomplished [27]. This can be verified by PL results shown in Fig. 7 that the extent of the fluorescence quenching is found to be noticeably increased with increasing GO weight ratio, indicating an significantly decreased the recombination of photogenerated electrons with holes in the composite photocatalyst. Moreover, the effective transfer of the photogenerated electrons from $ZnIn_2S_4$ to rGO through Zn—O—C bonds is beneficial for preventing the reduction of $In^{3+}$ and $Zn^{2+}$ by electrons, which increases the stability of $ZnIn_2S_4$ in the composite photocatalyst. Also, rGO can act as a protective layer to protect $ZnIn_2S_4$ against the dissolution of the photocatalyst, further improving the stability of $ZnIn_2S_4$. In addition, relatively high surface area of the composite can provide both high adsorption capability and high population of active sites. Thus, 4-NP molecules can be more easily concentrated near the catalyst surface and then the concentrated contaminant molecules environment over catalyst surface speed their reaction with photo-

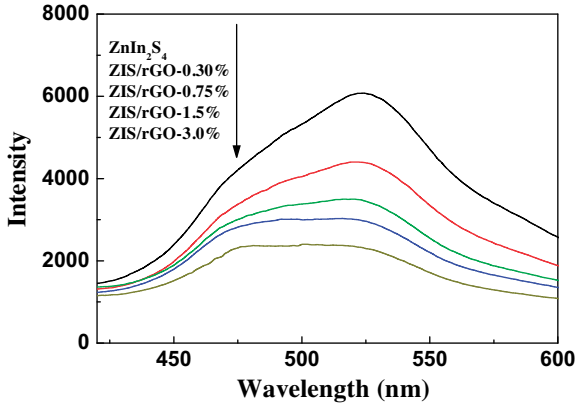


**Fig. 7.** PL spectra of $ZnIn_2S_4$ and ZIS/rGO composites.

generated active species (·OH, $O^{2-}$·, $h^+$, etc), which accelerates the photocatalytic degradation of 4-NP to produce different intermediates and then are finally mineralized to $CO_2$ and $H_2O$ with enough degradation time. However, the composites with too high amount of GO added (*e.g.*, ZIS/rGO–3.0%) will hinder the improvement of the photocatalytic performance owing to the adverse effect of high rGO modification ratio: (1) absorption of most of incident light by rGO rather than by $ZnIn_2S_4$; and (2) significant decrease of surface area of the composite resulting in the decrease of reaction active sites. Therefore, a suitable amount of GO modification is critically important to improve the photocatalytic performance.

## 4. Conclusion

In summary, a chemically cross-linked ZIS/rGO composite photocatalyst with enhanced sunlight-driven photocatalytic activity and stability are fabricated via an one-step hydrothermal method. The improved photocatalytic performance of the composite with an optimized amount of GO added is attributed to the synergistic effect of narrowed bandgap, positive valence band potential and superior electron transport property ascribed from the formation of Zn—O—C bonds as well as relatively high surface area. This study will motivate new developments in chemically cross-linked photocatalyst methodology and promote their practical application in environmental purification of organic contaminants in water.

## Acknowledgments

This work was financially supported by the Australian Research Council (ARC) Discovery Project, NSFC (21307132 and 41373102), NSFC – Guangdong Joint Funds(U1401245), National Natural Science Funds for Distinguished Young Scholars(41425015), Team Project of Natural Science Foundation of Guangdong Province, China (S2012030006604), Guangdong Natural Science Foundation(S2013040016408) and China Postdoctoral Science Foundation (2013M530378 and 2014T70829).

## Appendix A. Supplementary data

Supplementary data associated with this article can be found, in the online version, at http://dx.doi.org/10.1016/j.apcatb.2014.12.048.

## References

[1] L.X. Yang, S.L. Luo, Y. Li, Y. Xiao, Q. Kang, Q.Y. Cai, Environ. Sci. Technol. 44 (2010) 7641–7646.
[2] G.K. Zhang, Y.Y. Gao, Y.L. Zhang, Y.D. Guo, Environ. Sci. Technol. 44 (2010) 6384–6389.
[3] W.J. Wang, T.W. Ng, W.K. Ho, J.H. Huang, S.J. Liang, T.C. An, G.Y. Li, J.C. Yu, P.K. Wong, Appl. Catal. B – Environ. 129 (2013) 482–490.
[4] X.L. Liu, H.M. Zhang, X.D. Yao, T.C. An, P.R. Liu, Y. Wang, F. Peng, A.R. Carroll, H.J. Zhao, Nano Res. 5 (2012) 762–769.
[5] Y.H. Zhang, N. Zhang, Z.R. Tang, Y.J. Xu, ACS Nano 6 (2012) 9777–9789.
[6] H.T. Yu, S. Chen, X.F. Fan, X. Quan, H.M. Zhao, X.Y. Li, Y.B. Zhang, Angew. Chem. Int. Ed. 49 (2010) 5106–5109.
[7] W.J. Zhou, Y.H. Leng, D.M. Hou, H.D. Li, L.G. Li, G.Q. Li, H. Liu, S.W. Chen, Nanoscale 6 (2014) 4698–4704.
[8] W.J. Zhou, H. Liu, J.Y. Wang, D. Liu, G.J. Du, J.J. Cui, ACS Appl. Mater. Interfaces 2 (2010) 2385–2392.
[9] H. Zhang, R.L. Zong, Y.F. Zhu, J. Phys. Chem. C 113 (2009) 4605–4611.
[10] Z.X. Chen, D.Z. Li, W.J. Zhang, Y. Shao, T.W. Chen, M. Sun, X.Z. Fu, J. Phys. Chem. C 113 (2009) 4433–4440.
[11] X.L. Gou, F.Y. Cheng, Y.H. Shi, L. Zhang, S.J. Peng, J. Chen, P.W. Shen, J. Am. Chem. Soc. 128 (2006) 7222–7229.
[12] Z.B. Lei, W.S. You, M.Y. Liu, G.H. Zhou, T. Takata, M. Hara, K. Domen, C. Li, Chem. Commun. (2003) 2142–2143.
[13] L. Shang, C. Zhou, T. Bian, H.J. Yu, L.Z. Wu, C.H. Tung, T.R. Zhang, J. Mater. Chem. A 1 (2013) 4552–4558.
[14] B. Gao, L.F. Liu, J.D. Liu, F.L. Yang, Appl. Catal. B – Environ. 129 (2013) 89–97.
[15] Q. Huang, F. Kang, H. Liu, Q. Li, X.D. Xiao, J. Mater. Chem. A 1 (2013) 2418–2425.

[16] S. Huang, Y. Lin, J.H. Yang, Y. Yu, ACS Symp. Ser. 1140 (2013) 219–241.
[17] D. Li, M.B. Muller, S. Gilje, R.B. Kaner, G.G. Wallace, Nat. Nanotechnol. 3 (2008) 101–105.
[18] Y.B. Li, H.M. Zhang, P.R. Liu, D. Wang, Y. Li, H.J. Zhao, Small 9 (2013) 3336–3344.
[19] J.S. Lee, K.H. You, C.B. Park, Adv. Mater. 24 (2012) 1084–1088.
[20] Y.H. Zhang, Z.R. Tang, X.Z. Fu, Y.J. Xu, ACS Nano 4 (2010) 7303–7314.
[21] X.Q. An, J.C. Yu, F. Wang, C.H. Li, Y.C. Li, Appl. Catal. B – Environ. 129 (2013) 80–88.
[22] G.Z. Liao, S. Chen, X. Quan, H.T. Yu, H.M. Zhao, J. Mater. Chem. 22 (2012) 2721–2726.
[23] Q.J. Xiang, J.G. Yu, M. Jaroniec, J. Phys. Chem. C 115 (2011) 7355–7363.
[24] D.L. Zhao, G.D. Sheng, C.L. Chen, X.K. Wang, Appl. Catal. B – Environ. 111 (2012) 303–308.
[25] Y.H. Zhang, Z.R. Tang, X. Fu, Y.J. Xu, ACS Nano 5 (2011) 7426–7435.
[26] J. Du, X.Y. Lai, N.L. Yang, J. Zhai, D. Kisailus, F.B. Su, D. Wang, L. Jiang, ACS Nano 5 (2011) 590–596.
[27] H. Zhang, X.F. Fan, X. Quan, S. Chen, H.T. Yu, Environ. Sci. Technol. 45 (2011) 5731–5736.
[28] J. Zhou, G.H. Tian, Y.J. Chen, X.Y. Meng, Y.H. Shi, X.R. Cao, K. Pan, H.G. Fu, Chem. Commun. 49 (2013) 2237–2239.
[29] L. Ye, J.L. Fu, Z. Xu, R.S. Yuan, Z.H. Li, ACS Appl. Mater. Interfaces 6 (2014) 3483–3490.
[30] H.F. Li, H.T. Yu, S. Chen, H.M. Zhao, Y.B. Zhang, X. Quan, Dalton Trans. 43 (2014) 2888–2894.
[31] N. San, A. Hatipoglu, G. Kocturk, Z. Cinar, J. Photochem. Photobiol. A 146 (2002) 189–197.
[32] Q. Pan, J. Xie, S.Y. Liu, G.S. Cao, T.J. Zhu, X.B. Zhao, RSC Adv. 3 (2013) 3899–3906.
[33] R. Kumar, K. Jayaramulu, T.K. Maji, C.N.R. Rao, Chem. Commun. 49 (2013) 4947–4949.
[34] H. Wang, H.W. Tian, X.W. Wang, L. Qiao, S.M. Wang, X.L. Wang, W.T. Zheng, Y.C. Liu, Chem. Res. Chin. Univ. 27 (2011) 857–861.
[35] T.C. An, J.Y. Chen, X. Nie, G.Y. Li, H.M. Zhang, X.L. Liu, H.J. Zhao, ACS Appl. Mater. Interfaces 4 (2012) 5988–5996.
[36] H.W. Ma, J.F. Shen, M. Shi, X. Lu, Z.Q. Li, Y. Long, N. Li, M.X. Ye, Appl. Catal. B – Environ. 121 (2012) 198–205.
[37] H.M. Zhang, X.L. Liu, Y.B. Li, Q.F. Sun, Y. Wang, B.J. Wood, P.R. Liu, D.J. Yang, H.J. Zhao, J. Mater. Chem. 22 (2012) 2465–2472.
[38] Q. Zhang, C.G. Tian, A.P. Wu, T.X. Tan, L. Sun, L. Wang, H.G. Fu, J. Mater. Chem. 22 (2012) 11778–11784.
[39] O. Akhavan, Acs Nano 4 (2010) 4174–4180.
[40] M. Samadi, H.A. Shivaee, M. Zanetti, A. Pourjavadi, A. Moshfegh, J. Mol. Catal. A – Chem. 359 (2012) 42–48.
[41] V. Chandra, J. Park, Y. Chun, J.W. Lee, I.C. Hwang, K.S. Kim, ACS Nano 4 (2010) 3979–3986.
[42] Q. Peng, B. Gong, R.M. VanGundy, G.N. Parsons, Chem. Mater. 21 (2009) 820–830.
[43] K. Sayama, A. Nomura, T. Arai, T. Sugita, R. Abe, M. Yanagida, T. Oi, Y. Iwasaki, Y. Abe, H. Sugihara, J. Phys. Chem. B 110 (2006) 11352–11360.